Effect of growth time on solvothermal synthesis of vanadium dioxide for electrochemical supercapacitor application

N. M. Ndiaye [a], T. M. Masikhwa [a], B. D. Ngom [b], M. J. Madito [a], K. O. Oyedotun [a] J. K. Dangbegnon[a] and N. Manyala [a]*

[a] *Department of Physics, Institute of Applied Materials, SARChI Chair in Carbon Technology and Materials, University of Pretoria, Pretoria 0028, South Africa.*

[b] Laboratoire de Photonique et de Nano-Fabrication, Faculté des Sciences et Techniques Kabi (UCAD) B.P. 25114 Dakar-Fann Dakar, Senegal

*Corresponding author's email: ncholu.manyala@up.ac.za, Tel.: + (27)12 420 3549;

Fax: + (27)12 420 2516

Highlights

- The effect of growth time on the morphology and electrochemical results on VO_2.
- The grown VO_2 as a function of time show two monoclinic phases.
- 6 M KOH electrolyte was found to be the best electrolyte for VO_2 electrochemical performance.
- 6 h was found to be the optimum growth time for best physical and electrochemical results.

ABSTRACT

In this work, we report the time-dependent morphological evolution of the as-prepared vanadium dioxide (VO_2) and its electrochemical performance for supercapacitor applications. VO_2 with different morphologies (microspheres and nanosheets) were successfully synthesised by solvothermal method for time growth ranging from 2 h 30min to 12 h at a temperature of 200 °C. X-ray diffraction (XRD), Raman spectroscopy, scanning electron microscope (SEM), high resolution transmission electron microscopy (HRTEM), energy dispersive spectroscopy (EDS), gas adsorption/desorption analysis and X-ray photoelectron spectroscopy (XPS) were used to characterize the structure, morphology, composition and the oxidation state of the as-prepared samples. The electrochemical behaviour of the as-prepared VO_2 samples were analysed in a three-electrode cell configuration using 6 M KOH aqueous electrolyte. The VO_2 samples revealed monoclinic crystal structure (with VO_2 (B) monoclinic phase for the samples prepared for 4h and 6h and VO_2 (A) monoclinic phase for the samples grown for 2 h 30min and 12 h. The VO_2 samples grown for 4 h and 6 h displayed nanoflakes and nanosheets-like morphology, respectively, whereas VO_2 samples grown for 2 h 30min and 12 h revealed nanorods-like morphology. The 6 h grown sample also showed more porous structure leading to much higher specific surface area, pore volume and enhanced electrochemical performance with highest specific discharge capacity of 49.28 mA h g^{-1} at current density of 0.5 A g^{-1} and the corresponding specific capacitance of 663 F g^{-1} at a scan rate of 5 mV s^{-1} with excellent cycling stability as compared to others samples. Accordingly, the 6 h is considered to be optimal growth time for VO_2 nanosheets for considerable potential as an electrode material for supercapacitor applications.

Keywords: VO_2, Ostwald-ripening, nanosheets, solvothermal, supercapacitors, energy storage

Graphical abstract

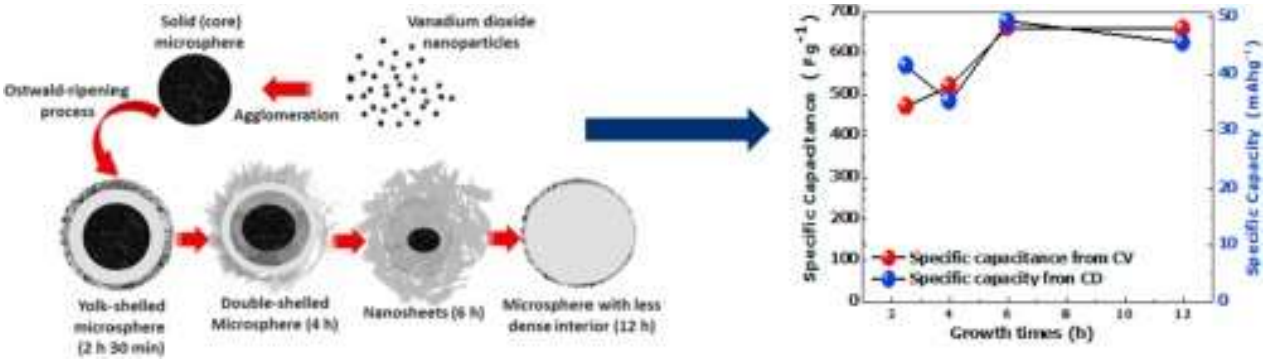

1. Introduction

The energy storage has become a key technological challenge due to the energy crisis and greenhouse effect in the past few decades [1,2]. The global scientific community has not only been developing strategies and rules for efficient energy generation and use, but has also been developing cutting-edge storage technologies to complement the energy production [3–5]. Supercapacitors (SCs), also called ultracapacitors or electrochemical capacitors (ECs) have been extensively explored in the field of energy storage compared with other storage devices such as dielectric capacitors, secondary cells and fuel cells. They exhibit higher power density and a broader range of working temperature compared to batteries, for example [6,7]. Moreover, SCs also exhibit longer cycling life and an enhanced efficiency for energy utilization hence they can store energy from various renewable energy sources such as solar energy, wind power and fast delivery on demand [8,9]. However, SCs suffer from low energy density [10], hence an improvement of their energy density will definitely increase their large-scale industrialization. In view of the energy storage mechanism, SCs can be divided into two types of capacitors, namely, electric double layer capacitors (EDLCs) that stores energy based on the electrostatic charge

accumulation on the surface between the electrode and electrolyte and faradaic supercapacitors mostly depend on fast and reversible faradic reactions to store energy [6]. Generally, the capacitive property and performance of SCs are influenced by both the electrolyte and electrode material [3,11,12]. In this work, our focus will be on designing better active faradic material for SCs.

The most common electrodes used for SCs are based on carbon materials. Although, such electrodes can deliver high power density with high cycling stability, most of their energy densities are still less than 10 W h kg^{-1} and this is related to the limitation of the charge storage mechanism involved for carbonaceous materials [13]. In other words, pure non-faradaic charge separation in an electric field gives rise to EDLC which is influenced by the active surface area of the material and its pore size distribution. The bulk of the carbon material is not involved in the charge storage and the charge stored on the surface could be drawn out rapidly, explaining the high power and low energy densities. Metal oxides have also been explored, especially on the sub-bulk where electrochemical redox or faradaic reactions occur. However, in contrast to carbon materials, in metal oxides a faradaic reaction involves to some extend the bulk (sub-bulk) of the material in charge storage. As a result, metal oxide electrode materials exhibit higher capacity, but at a slower discharge rate compared to carbon electrode materials. Therefore, by tuning the structural properties of the metal oxides, for instance, the morphology of the materials, the electrochemical performance could be enhanced. In view of this, vanadium oxides which have high faradaic activity, adopt different structures (VO, V_2O_3, V_2O_5, VO_2, V_3O_5, V_4O_7) due to their variable oxidation states and can easily be engineered to a two-dimensional structure are quite interesting to be investigated as electrodes for energy storage applications.

Currently, vanadium oxides have been widely investigated as electrode materials for supercapacitors. They can be modified with reduced graphene oxides [10], CNTs [14,15], conducting polymers [16]. It is worth mentioning that for one-electron redox reaction for VO_2, the theoretical specific capacity value is as high as 323 mA h g^{-1} [17]. Thus, this material can be an excellent candidate for energy storage application.

Furthermore, Deng *et al.* reported the graphene/VO_2 (RG/VO_2) hybrid material for high-performance electrochemical capacitor by hydrothermal reduction technology and the material exhibited a specific capacitance of 225 F g^{-1} at a current density of 0.25 A g^{-1} in 0.5 M K_2SO_4 aqueous solution [10]. Wang *et al.* prepared 3D graphene/VO_2 nanobelt for high-performance supercapacitors by hydrothermal strategy which exhibited a specific capacitance of 191 F g^{-1} at a current density of 1 A g^{-1} in 0.5 M K_2SO_4 aqueous solution [1]. Rakhi *et al.* reported VO_2 nanosheets electrodes in organic gel electrolyte for supercapacitor applications by hydrothermal method and the electrodes exhibited a specific capacitance of 405 F g^{-1} at a current density of 1 Ag^{-1} [18]. Xiao *et al.* reported the composite of metastable vanadium dioxide [VO_2(B)] nanobelts on reduced graphene oxide (RGO) layers by one-step hydrothermal process which exhibited a specific capacitance of 290.4 F g^{-1} at a current density of 0.2 A g^{-1} in 1 M Na_2SO_4 aqueous solution [19]. Liming *et al.* prepared VO_2/ordered mesoporous carbon (CMK-3) composites for hybrid capacitors by solid-state reaction process which exhibited a specific capacitance of 131 F g^{-1} in 1 M KNO_3 aqueous solution [20]. In brief, previously reported VO_2 based electrodes are mainly composites which exhibited specific capacitance values in the range of about 130 to 430 F g^{-1} [10,14,18,20,21], and were not evaluated in 6 M KOH as the electrolyte. In fact, to the best of our knowledge, no report exist on the electrochemical performance of VO_2 electrode in 6 M KOH aqueous electrolyte until the present. Usually, a choice of KOH is motivated by its high

ionic conductivity (i.e. with 73.5 and 198 S cm^2 mol^{-1} for K^+ and OH^-, respectively [22]) as compared to other neutral electrolytes [23,24].

Herein, we report the time-dependent morphological evolution of the as-prepared monoclinic VO_2(M) by a solvothermal method for supercapacitor applications. The synthetic route in this work for the synthesis of the VO_2 microspheres is similar to a novel route for synthesis and growth formation of metal oxides microspheres proposed by Y. Zhang et al. [25]. However, compared to the synthetic route proposed by Y. Zhang et al. [25] which uses the hydrothermal; our approach uses the solvothermal method at different growth times and temperatures. Different morphologies of VO_2 (i.e., microspheres and nanosheets) were successfully synthesised and the electrochemical performance of the samples were analysed in a three-electrode cell configuration using 6 M KOH aqueous electrolyte as a function of growth time. The as-prepared 6 h grown VO_2 nanosheets showed a significant improvement in the porous nature and exhibited enhanced electrochemical performance compared to VO_2 microspheres obtained from other growth times. The VO_2 nanosheets show a considerable potential as an electrode material for supercapacitor applications.

2. Experimental

2.1. Materials

Vanadium (V) oxide (V_2O_5, purity ≥ 98%), oxalic acid dehydrate ($C_2H_2O_4{\cdot}2H_2O$ purity 99%) and propan-2-ol ($CH_3CHOHCH_3$) were purchased from Sigma- Aldrich. Polycrystalline Nickel (Ni) foam (3D scaffold template with an areal density of 420 g m^2 and thickness of 1.6 mm was purchased from Alantum (Munich, Germany). Potassium hydroxide (KOH, min 85%) was purchased from Merck (South Africa).

2.2. Synthesis of VO_2 microspheres and nanosheets using solvothermal method

Scheme 1 shows the schematic view of the procedure used in the preparation of VO_2 sample for 2h 30 min growth time of which the similar procedure was repeated for other different growth times of 4, 6 and 12 h. Initially, bulk V_2O_5 powder (1.2 g) and $H_2C_2O_4{\cdot}2H_2O$ in a molar ratio of 1:3 were dissolved in 40 mL of deionized water under vigorous stirring at 80 °C for 3 h until a clear blue VOC_2O_4 solution (0.33 M) was formed. Then 6 mL of the obtained precursor VOC_2O_4 was added to 60 mL of isopropanol under vigorous stirring for 20 min at 80 °C. The final homogeneous solution was transferred into a sealed Teflon-lined stainless-steel autoclave and kept at a temperature of 200 °C for different growth time varying from 2 h 30 min to 12 h. After cooling to room temperature, the black powder was centrifuged, washed several times with deionized water and ethanol and dried at 60 °C for 6 h. The final product has different morphologies depending on the growth time as illustrate by SEM micrograph as the last image in scheme 1. Generally, the reactions to obtain VO_2 can be expressed as follows:

$$V_2O_5 + 3H_2C_2O_4 \rightarrow 2VOC_2O_4 + 2CO_2 + 3H_2O \quad (1)$$

$$VOC_2O_4 \rightarrow VO_2 + CO_2 + CO \quad (2)$$

Scheme 1. Preparation procedure of vanadium dioxide.

3. Structural, morphological and composition characterization

X-ray diffraction (XRD) spectra of the as-prepared VO_2 sample were collected using an XPERT-PRO diffractometer (PANalytical BV, Netherlands) with theta/2theta geometry, operating at 50 kV and 30 mA and reflection geometry at 2θ values ranging from 10 – 80° with a step size of 0.01°. Raman spectroscopy measurements were obtained using a T64000 micro-Raman spectrometer (HORIBA Scientific, Jobin Yvon Technology) with a 514 nm laser wavelength and spectral acquisition time of 120 s was used to characterize the as-prepared vanadium oxide samples. The morphology of the as-prepared VO_2 samples was studied using a high-resolution Zeiss Ultra Plus 55 field emission scanning electron microscope (FE-SEM) operated at a voltage of 2.0 kV. T High resolution transmission electron microscopy (HRTEM) micro-images was carried out with a JEOL JEM-2100F microscope operated at 200 kV (Akishima-shi, Japan). X-ray photoelectron spectroscopy (XPS, *K*-alpha, Thermo Fisher) with monochromatic Al Kα radiation as the X-ray source was used to irradiate the sample surface and determine the chemistry of the samples. Nitrogen adsorption–desorption isotherms were measured at -196 °C

using a Micromeritics ASAP 2020. All the samples were degassed at 180 °C for more than 12 h under vacuum conditions. The surface area was calculated by the Brunauer–Emmett–Teller (BET) method from the adsorption branch in the relative pressure range (P/P_0) of 0.01–1.0.

4. Electrochemical characterization

The electrochemical properties were studied using a Bio-Logic VMP-300 potentiostat in a three-electrode configuration controlled by the EC-Lab® V10.37 software. The vanadium dioxide material served as the working electrode, glassy carbon plate as the counter electrode and Ag/AgCl (3 M KCl) as the reference electrode in 6 M KOH electrolyte. The vanadium dioxide electrode was prepared according to the following steps: 85 wt.% of vanadium dioxide was mixed with 10 wt.% carbon black as conducting additive and 5 wt.% polyvinylidene difluoride (PVdF) binder in an agate mortar. The mixture was then dissolved with 1-methyl-2-pyrrolidinone (NMP) to form slurry. The slurry was then uniformly pasted on a nickel foam current collector and dried at 60 °C in an electrical oven for 8 h to ensure complete evaporation of the NMP. The masses of the materials pasted on the current collector were approximately 2 mg, for comparison sake. The cyclic voltammetry tests were carried out in the potential range of 0 to 0.5 V (vs. Ag/AgCl) at different scan rates ranging from 5 to 100 mV s^{-1}. The galvanostatic charge–discharge measurements were also carried out at different current densities from 0.5 to 10 A g^{-1} and the electrochemical impedance spectroscopy (EIS) measurements were done in the frequency range of 100 kHz–10 mHz in open circuit voltage. All the electrochemical tests were performed at room temperature.

5. Results and Discussion

5.1.Structural, morphological, and composition characterization

Fig. 1(a) shows the XRD patterns of the as-prepared vanadium dioxide samples grown at 200 °C for 2h 30 min, 4h, 6h and 12h, respectively. The XRD patterns of the as-prepared samples display diffraction peaks confirming the samples crystallinity. In Fig. 1(a), it can be seen that for a growth times of 2h 30 min, and 12 h, the XRD patterns are similar, while samples for a growth times of 4 h and 6h show similar XRD patterns as well. Although, the XRD patterns for the growth times of 4 h and 6h appear noticeably different from those of 2h 30 min and 12h, one is looking at the same material. Furthermore, the XRD patterns of the as-prepared vanadium dioxide samples grown for 2 h 30 min, 4 h, 6 h and 12 h were indexed to a monoclinic structure with different phases.

The XRD patterns of the vanadium dioxide samples grown for 2 h 30 min and 12 h can be indexed as VO_2 (A) monoclinic structure with a space group *P 1 2/m 1* and lattice parameters of a = 9.0600 Å, b = 5.8000 Å, c = 4.5217 Å, β=91.85° using the best matching inorganic crystal structure database (ICSD) card #1503 for VO_2, as shown in Fig. 1(b). The XRD patterns for growth times of 4h and 6h were indexed as VO_2 (B) monoclinic structure with a space group of *C 1 2/m 1*, lattice parameters of a = 12.03 Å, b = 3.693 Å, c = 6.42 Å, β = 106.1° using the best matching inorganic crystal structure database (ICSD) card #199, as shown in Fig. 1(c).

The noticeable difference in the crystallographic phases in the monoclinic structure of the grown vanadium dioxide samples, could be ascribed to preferential crystallographic growth orientation, influenced by the specific processes of structure evolution during the crystallization; nucleation, island growth, coalescence of islands, formation of polycrystalline islands and channels, development of a continuous structure, and grains growth. The evolution of the structure in

polycrystalline structure is a very complex phenomenon and exhibits different features at different stages during the grains growth.

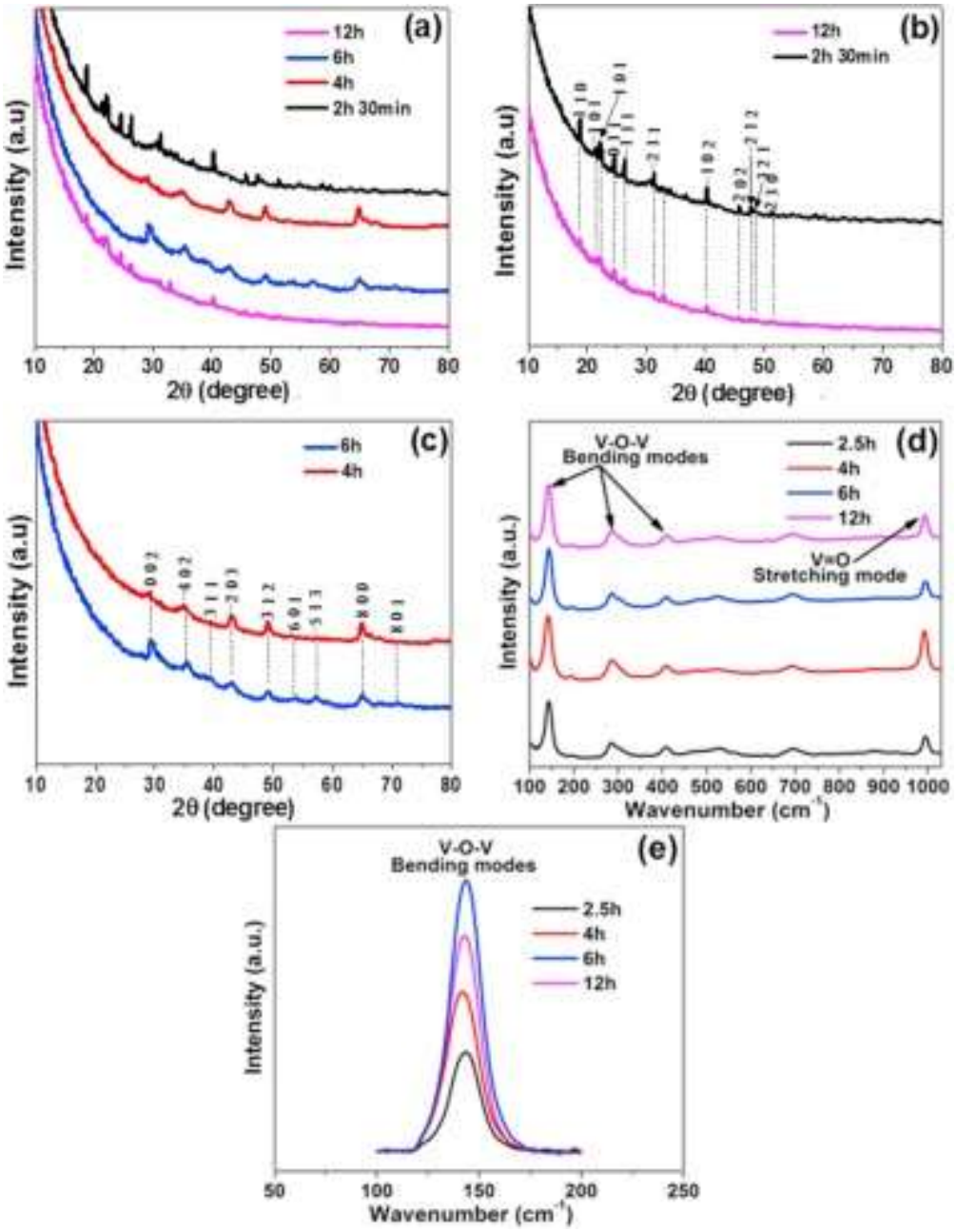

Fig .1: (a) The XRD patterns of the as-prepared vanadium dioxide samples grown at 200 °C for 2 h 30 min, 4, 6 and 12 h. The XRD patterns for samples grown at (b) 2 h 30 min and 12 h (c) 4 h and 6 h (d) The Raman spectra of the samples synthesized at growth times shown in the figure, and (e) a comparison of the intensity of the prominent Raman band at the different growth times.

A comprehensive description of the formation of these peculiar structural features is possible using the structure-forming phenomena mentioned above as a basis (nucleation, crystal growth, grain growth). These phenomena are composed of elementary atomic processes as reported by Ngom et al. [26], which can account for their global effects on the structure evolution. It is important to note that not only the temperature controls the atomic processes, but also the structural conditions characteristic of the actual growth stage.

To further confirm the phase of the as-prepared vanadium dioxide, the Raman spectra of the samples were obtained as shown in Fig. 1(d). For vanadium oxides, the Raman bands exist within the wavenumber range of ~100 - 400 cm^{-1}, ~400 - 800 cm^{-1} and 800 - 1100 cm^{-1} attributable to V−O−V bending modes, V−O−V stretching modes and V=O stretching modes respectively [27,28]. In addition, VO_2 monoclinic (VO_2 (M)) has prominent Raman band at approximately 145 cm^{-1} (V−O−V bending mode) [29,30]. As shown in Fig. 1(d), the Raman bands of as-prepared vanadium dioxide were mainly observed for V−O−V bending modes and V=O stretching mode suggesting that these modes are dominant in the prepared VO_2, and the prominent Raman band at ~145 cm^{-1} further suggests that the samples are predominantly VO_2(M) as expected. At low-frequency vibrations (wavenumber of ~100 cm^{-1}), the Raman bands typically originate from large-scale vibrations, such as the whole crystal lattice vibrating hence could be useful in distinguishing between amorphous and crystalline material or even between different crystalline forms (polymorphs). Of course, Raman scattering is sensitive to the degree of crystallinity in a sample [31]. Fig. 1(e) shows a comparison of the intensity of the prominent Raman band at ~145 cm^{-1} as a function of growth time. It can be seen that as growth time increases from 2h 30 min to 6 h the Raman intensity increases significantly suggesting an

enhancement in the crystallinity of the samples. The high-frequency Raman located ~ 1000 cm^{-1} is attributed to the terminal oxygen which results from an unshared oxygen. Prolonged growth time decreases the Raman intensity, as illustrated by the Raman spectrum of the sample prepared for 12 h. This could mean that the sample obtained for 4 h and 6 h growth times have a different crystallinity compared to others samples prepared for 2 h 30min and 12 h. This observation confirms our XRD findings on the different VO_2 monoclinic phases for the prepared samples. So one could suggest that the changes on the Raman intensity from 2 h 30min to 4h and from 6 h to 12 h are due to the changes in the monoclinic phases from VO_2(A) to VO_2(B) and vice versa.

Fig. 2(a) - 2(d) show SEM micrographs (low and high magnifications) of the samples grown at 200 °C for 2 h 30 min, 4 h, 6 h and 12 h, respectively. It can be seen that all the samples are composed of microspheres (see the insert figures), but the sample grown for 4 h is showing nanoflakes-like structure on the surface of the microspheres as compared to closed distinct microsphere surface morphology for the 2 h 30min grown sample which is composed of nanorods-like structure. In other words, for a growth time of 2 h 30min the surfaces of the microspheres show relatively shorter nanorods which are flat and more compact on the surfaces of the microspheres, while, for a growth time of 4 h the surface of the microspheres shows nanoflakes which are relatively perpendicular to the surfaces. It is worth mentioning that at this growth time of 4h the nanosheets-like structure starts developing and become noticeable at a longer growth time of 6h which clearly shows nanosheets-like morphology on the surface of the microspheres. However, for a longer growth time of 12 h the material shows microspheres surface morphology similar to that of 2 h 30min growth time but the nanorods are relatively perpendicular to the surface of the microspheres.

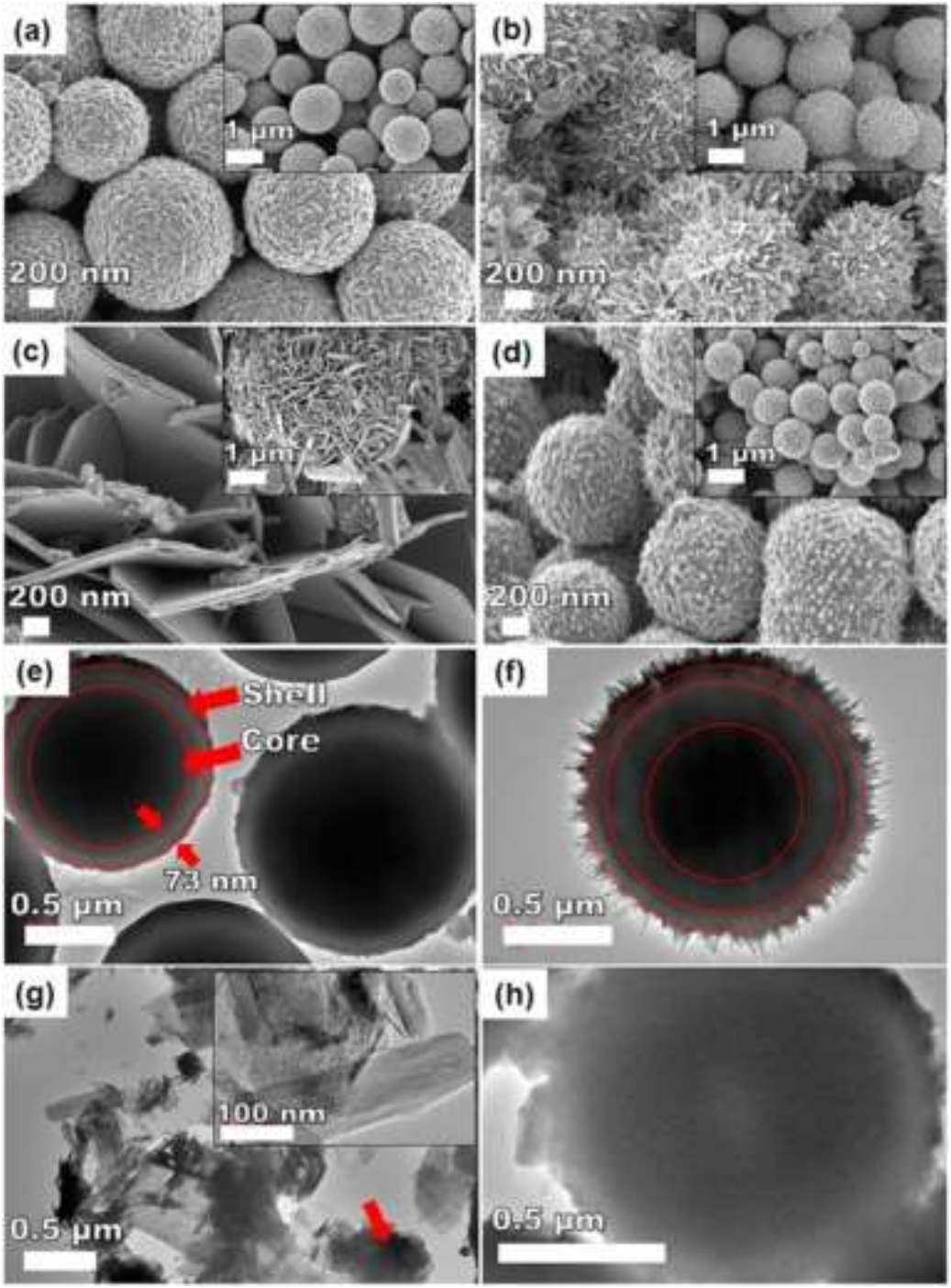

Fig. 2: The SEM images of the as-prepared vanadium dioxide samples grown at 200 °C for (a) 2 h 30 min, (b) 4 h, (c) 6 h and (d) 12 h. The insert figures show the corresponding low magnification micrographs. The corresponding TEM micrographs for growth time of (e) 2 h 30 min, (f) 4 h, (g) 6 h and (h) 12 h. The insert figure in (g) shows the high magnification micrograph.

The morphology of the samples was further confirmed by TEM as shown in Fig. 2 (e) to 2 (h). TEM micrographs for a growth time of 2 h 30min (Fig. 2(e)) and 4 h (Fig. 2(f)) clearly show the microspheres with distinct microsphere surface morphology. In this regards the surface of the microsphere for 4 h growth time shows nanoflakes in accordance with SEM results.

In Fig. 2(e), the interior structure of the microspheres reveals the yolk-shelled sphere-like with a gap distance of approximately 73 nm between the core and the shell, and for 4h the interior structure of the microsphere reveals the double-shelled microsphere. For further prolongation of the growth time, i.e. 6h, the nanosheets evolved, as shown in Fig. 2(g) and the formation of these nanosheets could be viewed as a coalescence from the nanoflakes observed on the surface of the microsphere for 4 h growth time which confirms the time-dependence grown from 4 h to 6 h with a noticeable change of the interior of the microsphere with time. In fact, the growth of the outer part of the microsphere consumes the inner substances (the core). The red arrow in Fig. 2(g) shows the core which has been consumed in the transformation of the interior of the microsphere to nanosheets. Furthermore, based on the morphology and the XRD results analysis a correlation could be made between these two findings. The obtained morphology could be correlated to the observed different VO_2 monoclinic phases. The 2 h 30min and 12 h growth times corresponding to the VO_2 monoclinic phase A give the same morphology with almost no time dependence effect, while the 4 h and 6 h growth times corresponding to the VO_2 monoclinic B phase show different morphology but with a time-dependence resulting from the coalescence of the nanoflakes seen on the sample prepared for 4 h that gives the nanosheets seen on the sample grown for 6 h. The difference on the morphology for the two different phases could be explained as result of the influence of the crystal growth on the final grains growth. It is well known that, crystals growing from the nuclei are randomly oriented due to the random

orientation of the nuclei themselves. The complete coalescence of the crystals touching each other constitutes grain coarsening, which also results in the development of discrete single crystals and is connected to some changes in the orientation controlled mainly by the minimization of the crystals interface energy. But, the observed morphology evolution of the as-prepared vanadium dioxide samples for 4h and 6h is well-thought-out to emerge from the inside-out Ostwald ripening process as depicted in scheme 2. Firstly, vanadium dioxide nanoparticles are formed and aggregated to form solid (core) microsphere which undergoes the inside-out Ostwald-ripening process and transform to the yolk-shelled microsphere. Upon further prolongation of the growth time, the secondary Ostwald-ripening process takes place on the initial solid core, resulting in the formation of the double-shelled microsphere with nanoflakes on the surface. The nanoflakes on the microsphere surface evolved into nanosheets upon longer growth time by consuming the inner core through coalescense. In fact, under hydrothermal conditions, the particles on the outer surface grow relatively easy because the recrystallization preferentially occurs at the solid–liquid interface [32].

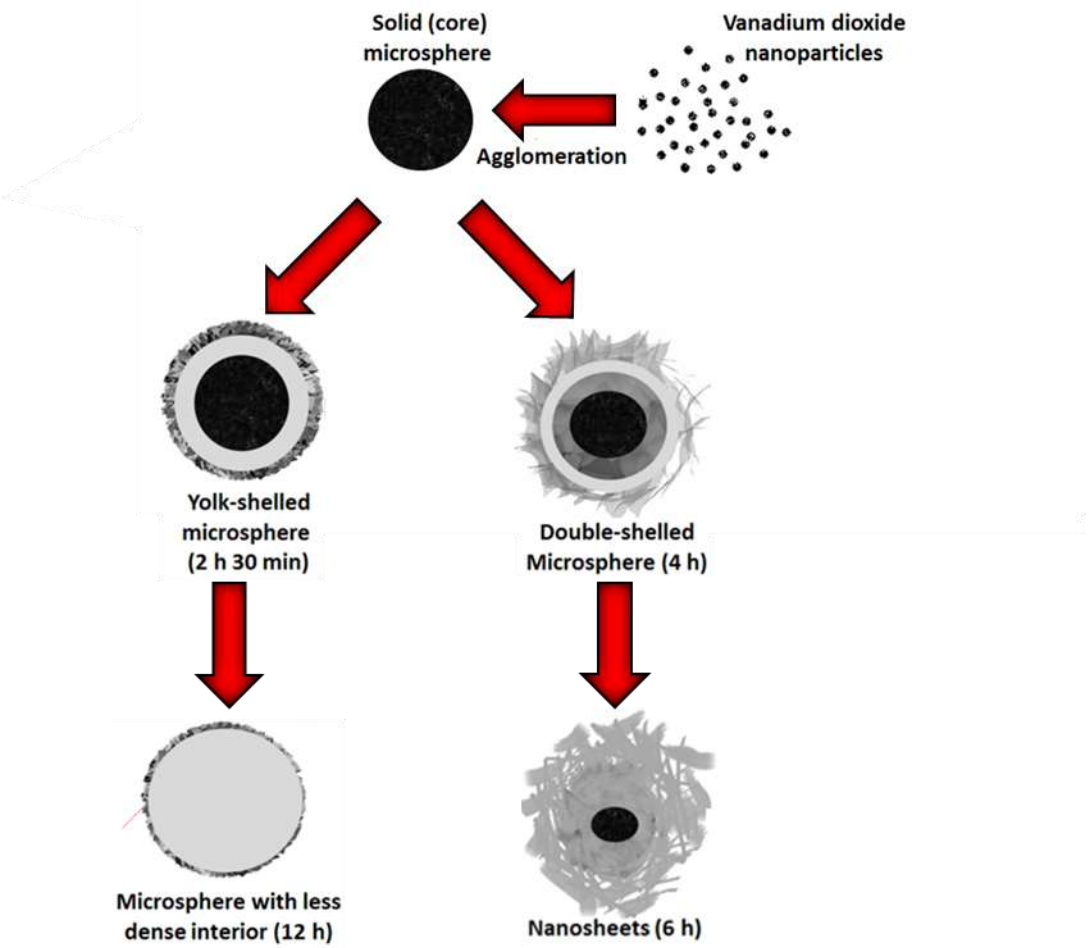

Scheme 2. Schematic illustration of the growth time-dependent morphological evolution of the as-prepared vanadium dioxide.

The vanadium oxidation state of the as-prepared vanadium dioxide was analysed by XPS, since the binding energy of the V $2p_{3/2}$ is dependent on the vanadium cationic oxidation state [33]. Fig. 3(c) shows the wide scan XPS spectrum of the as-received (i.e., without sputter cleaning) vanadium dioxide grown for 6 h. Similar to EDS, the wide scan XPS spectrum displays the main elements, V (23.48 at%) and O (49.51 at%) of the sample, and the observed C (27.01 at%) may be due to contamination from the precursor and/or the surface-adsorbed CO_2 and O_2. The core level spectrum of V 2p reveals the binding energy peaks at 524 eV and 516 eV which correspond to the V $2p_{1/2}$ and V $2p_{3/2}$ core levels, respectively, as shown in Fig. 3(d) [33]. The core level

spectrum of V 2p suggests that the oxidation state of the as-prepared vanadium dioxide is predominantly V^{4+}.

The surface area and the pore size distribution of the as-prepared vanadium dioxide were analysed by BET. Fig. 3(e) and 3(f) show the N_2 gas isotherms and pore size distribution obtained using Barrett-Joyner-Halenda (BJH) method, respectively for the as-prepared vanadium dioxide samples. The nitrogen adsorption-desorption isotherm of the vanadium dioxide shows a type III isotherm with H3 hysteresis, indicating a weak interaction between the N_2 adsorbent and the material and the hysteresis indicating non-rigid aggregates of plate-like particles or assemblages of slit-shaped pores. From Fig. 3(e) the specific surface area (SSA) was calculated as 16.0, 23.82, 34.14 and 25.12 $m^2 g^{-1}$ for vanadium dioxide samples grown for 2 h 30 min, 4, 6 and 12 h, respectively. Fig. 3(f) shows a concentration of pore volume ranging from ~5 to 20 nm, signifying that the pores which exist in these materials are predominantly meso-pores. Consequently, the BET results reveal that the sample grown for 6 h has larger SSA and high pore volume which would provide the probability of efficient transport of electrons and ions facilitating the electrolyte ion diffusion and deliver more electroactive sites for fast energy storage through redox reaction, contributing to higher electrochemical capacity.

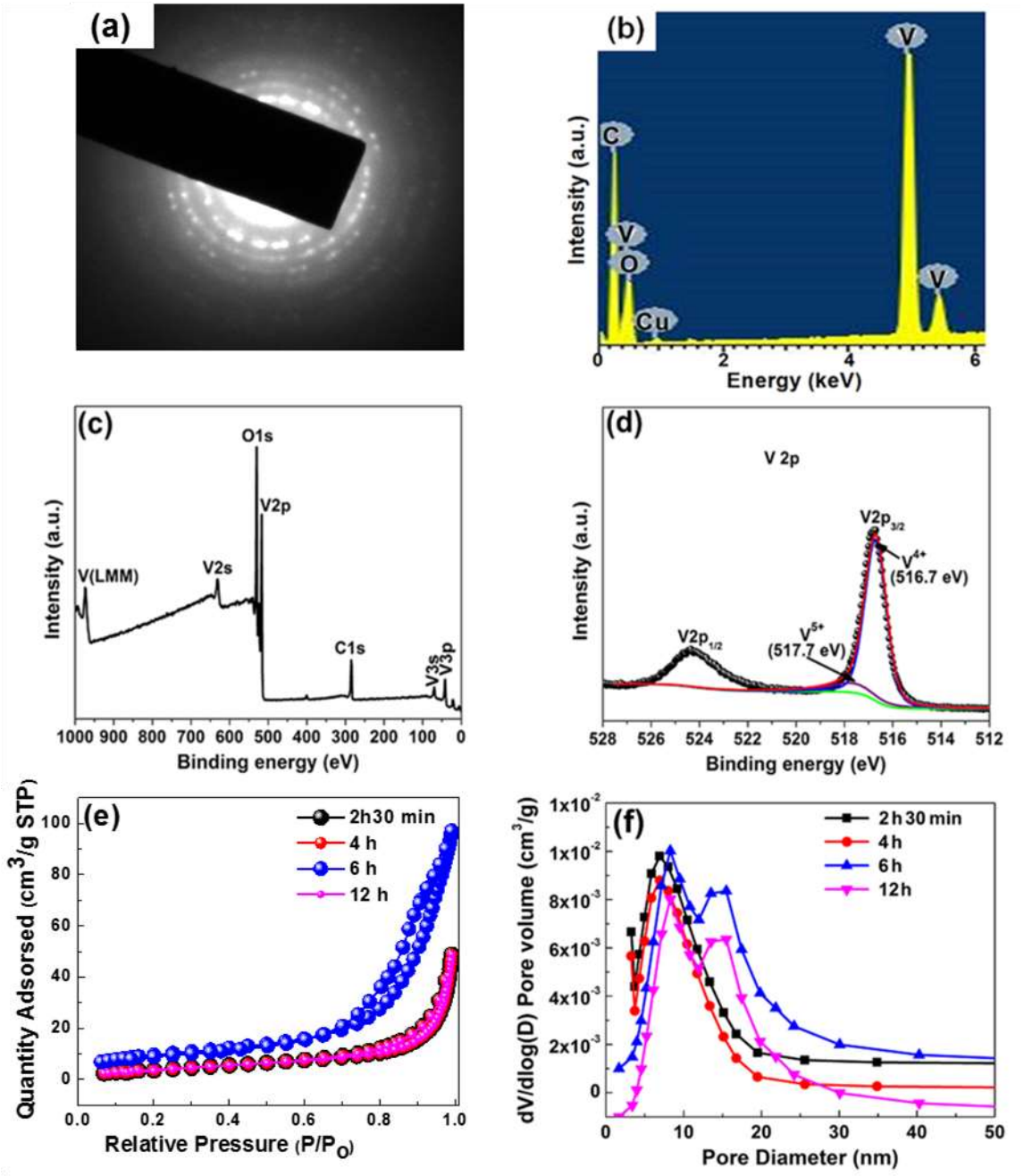

Fig. 3: (a) The selected area electron diffraction (SAED) pattern of the as-prepared vanadium dioxide sample grown at 200 °C for 6 h and (b) the EDS spectra of the vanadium dioxide grown at 200 °C for 6 h. (c) The wide scan XPS spectrum of the as-received (i.e., without sputter cleaning) vanadium dioxide grown at 200 °C for 6 h, and (d) the corresponding core level spectrum of V 2p. (e) N_2 absorption/desorption isotherms; and (f) pore size distribution of vanadium dioxide samples grown at 200 °C for 2 h 30 min, 4, 6 and 12 h.

5.2.Electrochemical performances of vanadium oxide

To evaluate the supercapacitive performance of the as-prepared vanadium dioxide samples we performed the cyclic voltammograms (CVs), galvanostatic charge-discharge (GCD) and electrochemical impedance spectroscopy (EIS) in a three-electrode half-cell configuration using 6 M KOH aqueous electrolyte. Fig. 4(a) shows the CV curves acquired at a scan rate of 50 mV s^{-1} within a potential range of 0.0 - 0.5 V for all electrode materials. These CV curves show a pair of redox peaks corresponding to the anodic peak at ~ 0.15 V and cathodic peak ~0.35 V, indicating the conventional behaviour of a battery-type electrode. The results suggest that the CV curves are mainly based on a redox mechanism of V^{4+} to V^{5+} which takes place at the surface of the VO_2 material according to the following reaction [22].

$$VO_2 + OH^- \leftrightarrow VO_2(OH) + e^- \quad (3)$$

It can also be clearly seen that the electrode made of the sample grown for 6 h exhibits better current response as compared to the other electrode materials grown at different times. This could be related to the higher degree of crystallinity of this sample which could enhance its electrical conductivity, but also to its higher SSA providing more sites for the redox reaction to occur.

Fig. 4(b) shows the overlaid GCD curves acquired at a current density of 0.5 Ag^{-1} for all vanadium dioxide electrodes. Beside the typical non-linear charge-discharge curves observed for faradaic capacitors, the discharge time for the electrode material grown for 6 h is significantly longer than the other electrode materials, signifying better rate of discharge. This is in good agreement with the CV curves in Fig. 4(a) and could be related to the same reasons for the high current response of the CV. This electrode was further characterized to understand its electrochemical performance. In other words, detailed CV and GCD measurements of this

electrode were carried out at scan rates ranging from 5 to 100 mV s^{-1} and current densities ranging from 0.5 to 10 Ag^{-1}, respectively. Fig. 4(c) shows the CV of this electrode at scan rate range of 5 - 100 $mV.s^{-1}$.

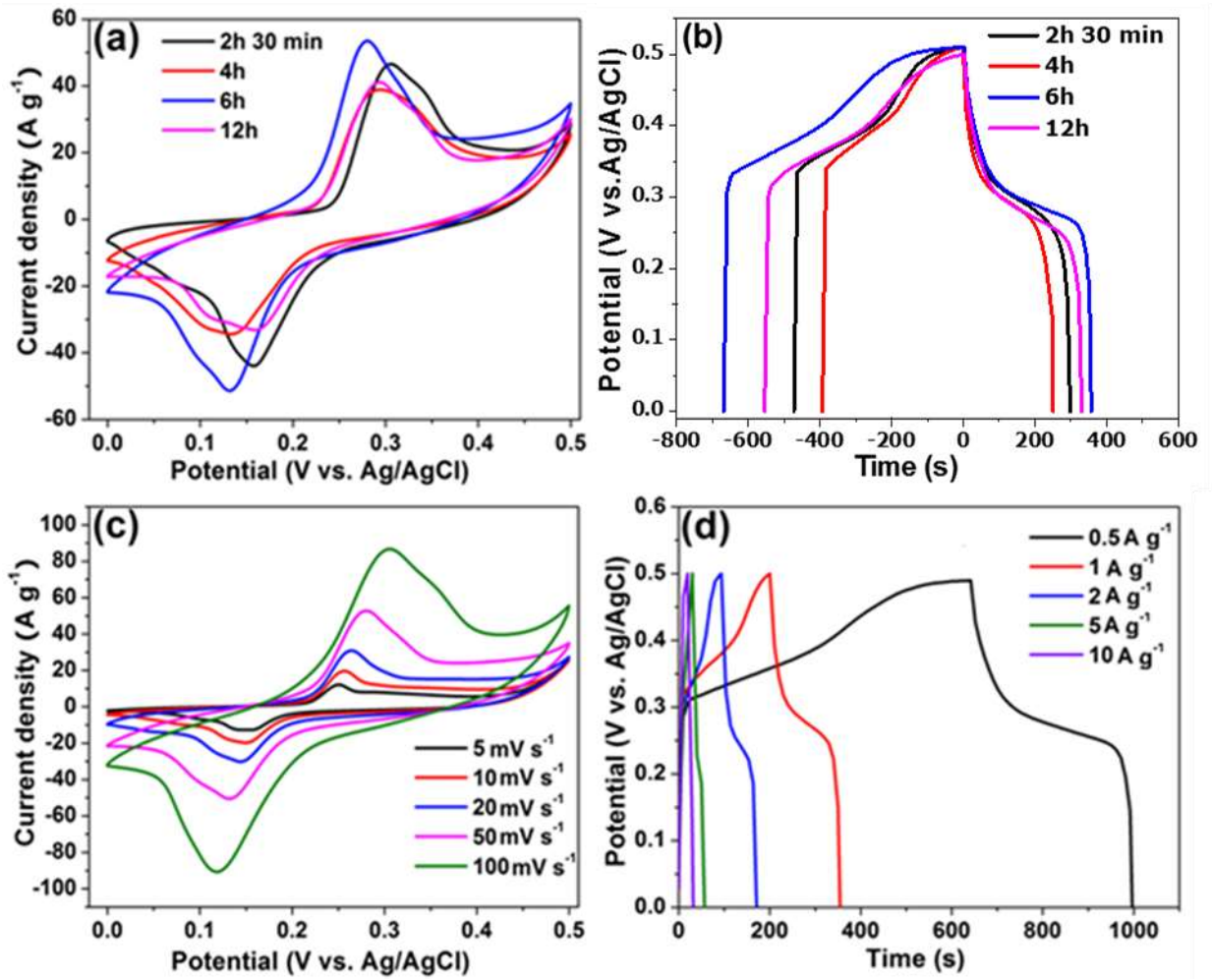

Fig.4: The comparison of (a) The CV curves acquired at a scan rate of 50 mV s^{-1} within a potential range of 0.0 to 0.5 V, (b) the GCD curves for all vanadium dioxide samples grown at 200 °C at a current density of 0.5 Ag^{-1}, (c) CV curves versus scan rate and (d) GCD curves versus as function of current density respectively.

It can be seen that the CV curves maintain a similar shape even at a high sweep rate, demonstrating the excellent reversible process and fast diffusion of electrolyte ions into the vanadium nanosheets. This also signifies that the kinetics of the interfacial faradic reactions and

the rate of electronic transport are fast enough at these scan rates [34] .Fig. 4(d) shows the charge-discharge curves at different current densities in the potential window of 0.0 to 0.5 V for the electrode material grown for 6 h, which shows the same faradaic charge-discharge behaviour for different current densities. Typical reduction in discharge time with increasing current density is also observed, which is related to the limited access to the electrolyte ions to the surface of the electrode material at high current density.

Based on the CV and GCD curves, the specific capacitance, C_S (F g^{-1}) and the specific capacity q_s (mA h g^{-1}) were calculated using the following equations (4) for CV curves and (5) for CD curves, respectively [35,36]:

$$C_S = \frac{1}{mv\,(V_f - V_i)} \int_{V_i}^{V_f} I(V)\,dV \qquad (4)$$

$$q_s = \frac{It}{3.6.m} \qquad (5)$$

where V is the potential window, v is the scan rate (V s^{-1}), V_f and V_i are the integration potential limits of the CV curve , I is the discharge current (A), m is the active mass of the electrode material (g) and t is the discharge time (s).

The plot of the specific capacitance and specific capacity as a function of growth time is shown in Fig. 5(a), respectively, for all electrodes. Overall, the specific capacity increasing with increasing growth time from 2 h 30 min to 6 h, thereafter decrease with increase growth time (to 12 h) showing that 6 h growth time is optimum growth time. In other words, in both measurements, the electrode grown for 6 h exhibits higher specific capacitance and capacity values as compared to the other electrodes. A decrease in these values for the electrode grown

for 12 h confirms that 6 h is indeed the optimum growth time. In brief, the sample grown for 6 h shows better capacitive performance, due to a more diffuse structure and large SSA of the nanosheets which can provide large electrochemical active sites and easy access for the electrolyte ions. However, for prolonged growth time (i.e., 12 h), the specific capacity and capacitance decrease because of the microsphere structure of the electrode which has reduced SSA limiting the OH^- ion diffusion into the electrode surface. In Fig. 5(b) and 5(c), the specific capacitance and capacity gradually decrease with increasing current density and scan rate, due to the decrease of effective interaction between the ions and the electrode at higher current density and sweep rate [37]. To further evaluate the conductivity of the electrode materials, the electrochemical impedance spectroscopic (EIS) measurement was carried out at an open potential and within a frequency range of 100 kHz - 10 mHz (Fig. 5(d)). At high frequency, the intercept with the $Z^{'}$ represents the equivalent series resistance (R_S) attributed to the diffusion of ions to/from the interface between the electrode and electrolyte [38]. As shown in Fig. 5(d), the electrode material grown for 6 h exhibits the shorter diffusion length as well as smaller R_S value of 0.42 Ω (Fig. 5(e)) due to the easiness of the movement of ions and the charge transfer towards the electrode/electrolyte interface.

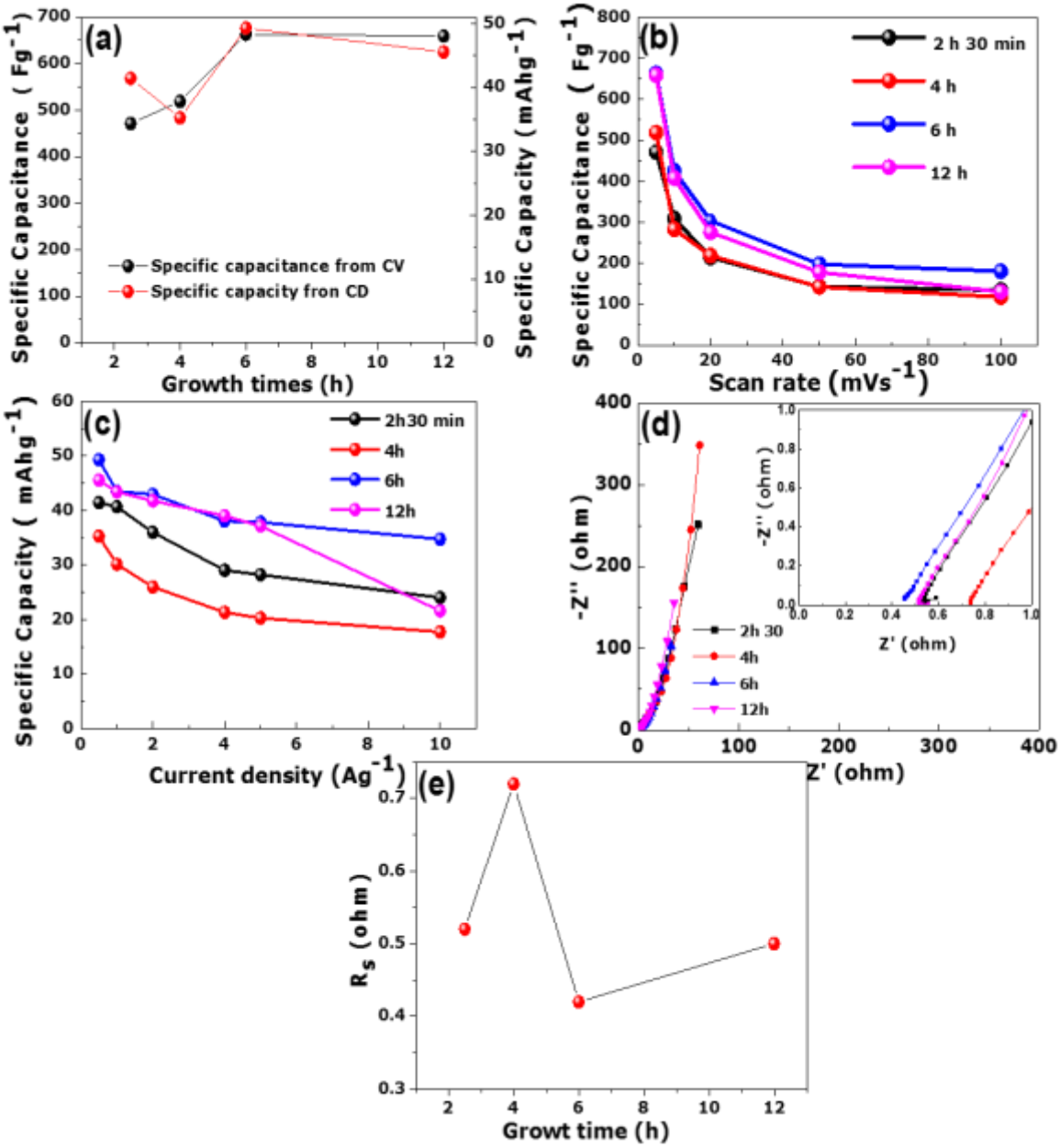

Fig. 5: (a) comparison of specific capacitance and specific capacity of vanadium dioxide at a scan rate of 5 mV s^{-1} and current density of 0.5 A/g, respectively (b) specific capacitance vs. scan rate, (c) specific capacity vs. current density, (d) EIS of vanadium dioxide samples grown at different times shown in the figure. The inset to (d) is the magnified plot showing the R_S values for different electrodes. (e) Equivalent series resistance (R_S) of vanadium dioxide samples grown at different times shown in the main figure.

Table 1 presents a summary of the pore size distribution, specific capacitance, specific capacity and the solution resistance for the as-prepared vanadium dioxide electrode materials grown at 200 °C with different growth times. It can be seen in table 1 that there is a clear correlation among different parameters such as SSA, micropore volume, R_s, C_s, and q_s that 6 h samples is always showing the best results. In other words this a clear evidence that the sample grown for 6 h is the best performing samples which makes this growth time to be optimum for producing VO_2 electrode material with the excellent physical and electrochemical properties.

Table 1. A summary SSA, micropore volume, R_s, C_s and q_s for all electrode materials

Growth time	**SAA ($m^2 g^{-1}$)**	**Micropore volume ($cm^3 g^{-1}$)**	**R_S (Ω)**	**C_S (Fg^{-1}) at 0.5 A g^{-1}**	**q_s ($mAhg^{-1}$)**
2 h 30 min	16.00	0.14	0.52	471.30	41.42
4 h	23.82	0.11	0.72	518.92	35.24
6 h	**34.14**	**0.19**	**0.42**	**663.22**	**49.28**
12 h	25.12	0.16	0.50	659.31	45.55

Furthermore, the cycling performance is an important factor in determining the supercapacitor electrodes for practical applications. To evaluate the cycle behaviour of the vanadium dioxide nanosheets structure (i.e. a sample grown for 6 h), the sample was subjected to 5000 cycles at current density of 10 A g^{-1}, as shown in Fig. 6(a). It can be seen that the sample shows good cycle stability with 99.4% coulombic efficiency up to 5000 charge-discharge cycles, signifying good electrochemical stability of the active material. Furthermore, an increase in the capacity retention with cycle number is also observed. This means that more accessible sites were made available during cycling without significant deterioration of the electrode material. Fig. 6(b)

shows the Nyquist plots of the sample grown for 6 h, before and after the last cycle recorded in the frequency range of 100 kHz to10 mHz. Both plots show similar curves with similar R_S values of 0.42 and 0.45 Ω before and after cycling, respectively and much shorter diffusion length after cycling which the indication that the electrode has been somehow improved after cycling. To further asses the cycle of the electrode material, the CV curves at a scan rate of 50 mV s^{-1} were obtained before and after cycling, as shown in Fig. 6(c). A shift in the redox peak current is observed after stability. This is tentatively related to a variation of the pH of the electrolyte due to the consumption of the OH^- or deposition of KOH during the stability test. This could decrease the pH of the solution, engendering the shift observed here [39]. This shift is followed by an increase in current response suggesting excellent cycling stability and highly reversible redox reaction of the vanadium dioxide, confirming results obtained in Fig. 6(a).

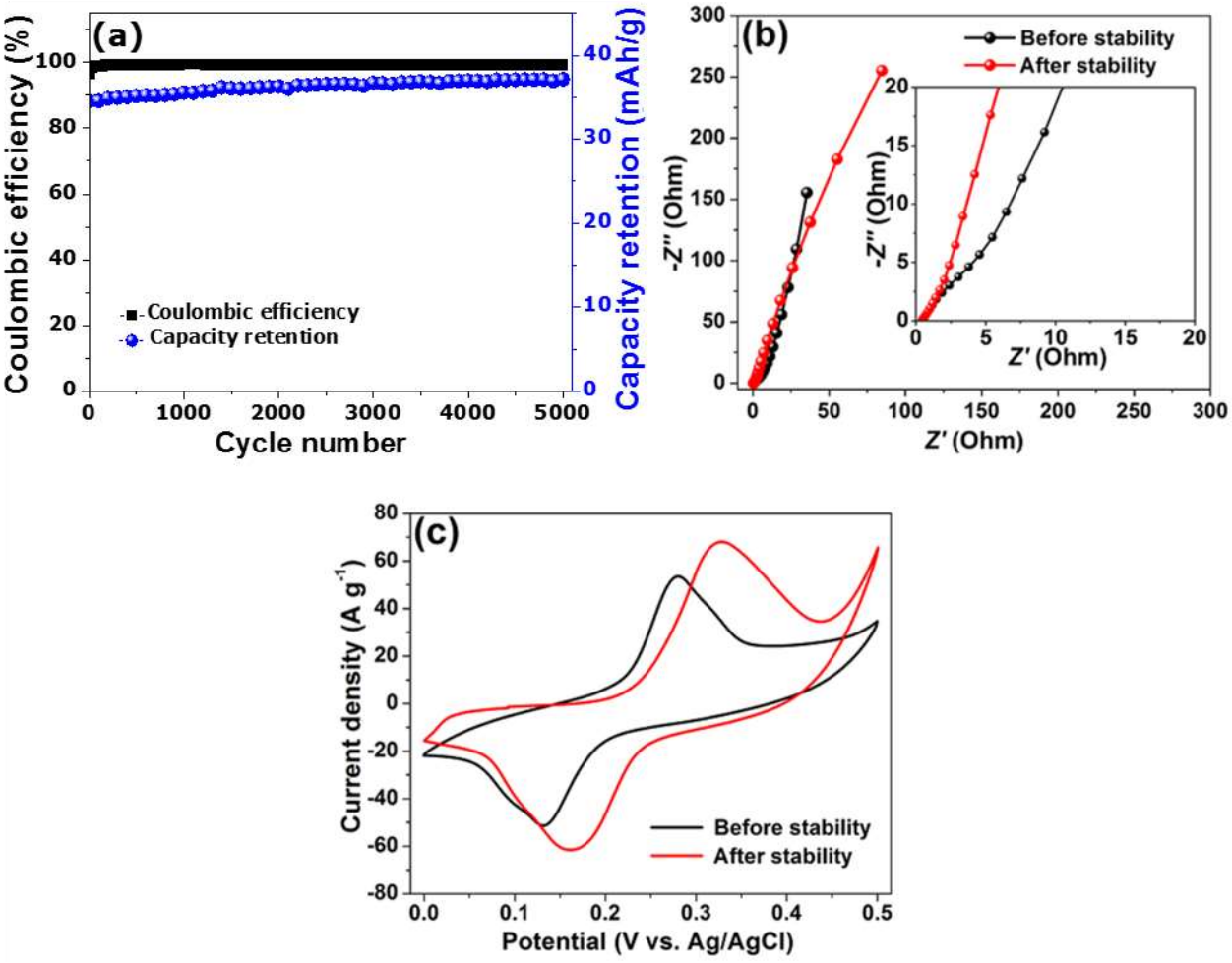

Fig .6: (a) Coulombic efficiency as a function of cycle number at a current density of 10 A g^{-1}, (b) Nyquist plot before and after cycling and (c) cyclic voltammetry before and after cycling for vanadium dioxide sample grown at 200 °C for 6 h.

Our results were also compared with other vanadium dioxide electrode materials in table 2. This work shows significant improvement on the specific capacitance of vanadium dioxide electrode compared with the vanadium dioxide-based electrode materials listed in table 2. However, it is worth mentioning that all the previous works were done in neutral electrolytes, which generally give a pseudocapacitor behaviour with extended voltage windows. In fact, different redox

reactions may occur when changing from a neutral electrolyte to a more alkaline electrolyte which could narrow the voltage window. But the low ionic conductivity of these neutral electrolytes hampers the specific capacitance value, as shown in this table.

Table 2. A comparison of specific capacitance obtained in this work and other previously published reports.

Electrodes	**Methods**	**Electrolytes**	**Specific capacitance (F g^{-1})**	**Capacitance retentions**	**References**
RG(1.0) / VO_2	One-step simultaneous hydrothermal reduction technology	0.5 M K_2SO_4	225 @ 0.25 A g^{-1}	65% after 1000 cycles @ 5 A g^{-1}	[10]
VO_2			136 @ 0.25 A g^{-1}	47% after 1000 cycles @ 5 A g^{-1}	
Gr/VO_2	One-step hydrothermal strategy	0.5M K_2SO_4	426 @ 1 A g^{-1}	92% after 5000 cycles @ 10 A g^{-1}	[1]
VO_2 nanobelts			243 @ 1 A g^{-1}	59% after 5000 cycles @ 10 A g^{-1}	
VO_2 nanosheets	Hydrothermal	Gel electrolyte	405 @ 1 A g^{-1}	82% after 6000 cycles @ 10 A g^{-1}.	[18]
VO_2(B)/RG	One step hydrothermal	1 M Na_2SO_4	290.4 @ 0.2 A g^{-1}	82.3% after 1000 cycles @ 2 A g^{-1}	[19]
VO_2			–	37.9% after 1000 cycles @ 2 A g^{-1}	

VO_2/CMK-3	Solid-state reaction	1 M KNO_3	131 (current density not given)	–	[20]
VO_2(B)/WCNTs	Sol–gel method assisted with freeze-drying	1M Na_2SO_4	250 @ 0.5 A g^{-1}	71% after 200 cycles @ 10 A g^{-1}	[14]
VOx @ carbon	One-step method using phenolic	1 M KNO_3	171 @ 100 mA g^{-1}	–	[21]
VOx			88 @ 100 mA g^{-1}		
VO_2-6 h nanosheets	**Solvothermal**	**6 M KOH**	**663 @ 5 mV s^{-1}**	**99.4% after 5000 cycles @ 10 Ag^{-1}**	**This work**

6. Conclusions

In this work, the time-dependent morphological evolution of the as-prepared monoclinic VO_2(M) through solvothermal method with growth time varied from 2 h 30 min to 12 h had been studied. In addition, the electrochemical performance of the as-prepared monoclinic VO_2 for supercapacitor applications was evaluated in a three-electrode cell configuration using 6 M KOH aqueous electrolyte. The VO_2 sample grown for 6 h displayed nanosheets-like morphology compared to other VO_2 samples grown for 2 h 30 min, 4 and 12 h which revealed microsphere-like morphology. Furthermore, the 6 h sample showed the best results for all measuerments carried out. This sample showed best specific surface area and pore volume, enhanced electrochemical performance with highest specific discharge capacity of 49.28 mA h g^{-1} at current density of 0.5 A g^{-1} and the corresponding specific capacitance of 663 F g^{-1} at a scan rate

of 5 mV s^{-1}. The samples also showed 99.4% coulombic efficiency up to 5000 charge-discharge cycles at current density of 10 A g^{-1}. Accordingly, the VO_2 nanosheets (6 h sample) show a considerable potential as an electrode material for supercapacitor applications.

ACKNOWLEDGEMENTS

This research was supported by the South African Research Chairs Initiative (SARChI) of the Department of Science and Technology and the National Research Foundation (NRF) of South Africa (Grant No. 61056). Any idea, finding, conclusion or recommendation expressed in this material is that of the author(s). The NRF does not accept any liability in this regard. N. M. Ndiaye thanks 'Organization for Women in Science for the Developing World (OWSD)' for financial support. N. M. Ndiaye acknowledges NRF through SARChI in Carbon Technology and Materials and University of Pretoria for financial support.

References

[1] H. Wang, H. Yi, X. Chen, X. Wang, D.W. Liu, J. Liu, G.Z. Cao, P.M. Ajayan, F. Wei, J. Mater. Chem. A., 2 (2014) p 1165–1173.

[2] J.W. Lee, A.S. Hall, J.D. Kim, T.E. Mallouk, Chem. Mater., 24 (2012) p 1158–1164.

[3] C. Liu, F. Li, L.-P. Ma, H.-M. Cheng, Adv. Mater., 22 (2010) p E28--E62.

[4] S.Chu. and A. Majumdar, Nature., 488 (2012) p 294–303.

[5] J. Yang, T. Lan, J. Liu, Y. Song, M. Wei, Electrochim. Acta., 105 (2013) p 489–495.

[6] P. Simon, Y. Gogotsi, Nat. Mater., 7 (2008) p 845–854.

[7] J. Chmiola, C. Largeot, P.L. Taberna, P. Simon, Y. Gogotsi, Science. (80)., 328 (2010) p. 480–483.

[8] M.F.E.-K. and R.B. Kaner, Nat. Commun. 4., (2013) p. 1475

[9] J. Miller, P. Simon, Sci. Mag., 321 (2008) p. 651–652.

[10] L. Deng, G. Zhang, L. Kang, Z. Lei, C. Liu, Z.-H. Liu, Electrochim. Acta., 112 (2013) p 448–457.

[11] L.L. Zhang, X.S. Zhao, P.L. Taberna, P. Simon, D. Plee, M. Mastragostino, S. Passerini, D. Zhao, M. Yumura, S. Iijima, Chem. Soc. Rev., 38 (2009) p 2520.

[12] E. Frackowiak, Phys. Chem. Chem. Phys., 9 (2007) p 1774.

[13] H.-Y. Li, C. Wei, L. Wang, Q.-S. Zuo, X. Li, B. Xie, M. Wu, L.-H. Chen, B.-L. Su, J. Chen, C.G. Hu, Y.X. Tong, J. Zhou, Z.L. Wang, Z.L. Wang, Y.L. Chueh, Z.L. Wang, J. Zhou, J. Mater. Chem. A., 3 (2015) p 22892–22901.

[14] L. Liang, H. Liu, W. Yang, J. Alloys Compd., 559 (2013) p 167–173.

[15] M. Sathiya, A.S. Prakash, K. Ramesha, J.M. Tarascon, A.K. Shukla, , J. Am. Chem. Soc., 133 (2011) p 16291–16299.

[16] L. Mai, F. Dong, X. Xu, Y. Luo, Q. An, Y. Zhao, J. Pan, J. Yang, Nano Lett., 13 (2013) p 740–745.

[17] X. Xia, D. Chao, C.F. Ng, J. Lin, Z. Fan, H. Zhang, Z.X. Shen, H.J. Fan, , Mater. Horiz., 2 (2015) p 237–244.

[18] R.B. Rakhi, D.H. Nagaraju, P. Beaujuge, H.N. Alshareef, Electrochim. Acta., 220 (2016) p 601–608.

[19] X. Xiao, S. Li, H. Wei, D. Sun, Y. Wu, G. Jin, F. Wang, Y. Zou, J. Mater. Sci. Mater. Electron., 26 (2015) p 4226–4233.

[20] L. Hu, L. Yu, C. Zhao, X. Long, W. Chen, J. Wuhan Univ. Technol. Sci. Ed., 25 (2010) p 574–578.

[21] C. Zhao, J. Cao, Y. Yang, W. Chen, J. Li, J. Colloid Interface Sci., 427 (2014) p 73–79.

[22] Y.-G. Wang, L. Cheng, Y.-Y. Xia, J. Power Sources., 153 (2006) p 191–196.

[23] D. Jiménez-Cordero, F. Heras, M.A. Gilarranz, E. Raymundo-Piñero, Carbon N. Y., 71 (2014) p 127–138.

[24] H. Wu, X. Wang, L. Jiang, C. Wu, Q. Zhao, X. Liu, B. Hu, L. Yi, , J. Power Sources., 226 (2013) p 202–209.

[25] Y. Zhang, C. Huang, C. Meng, T. Hu, Mater. Chem. Phys., 177 (2016) p 543–553.

[26] B.D. Ngom, M. Chaker, A. Diallo, I.G. Madiba, S. Khamlich, N. Manyala, O. Nemraoui, R. Madjoe, A.C. Beye, M. Maaza, Acta Mater., 65 (2014) p 32–41.

[27] F.D. Hardcastle, I.E. Wachs, , Solid State Ionics., 45 (1991) p 201–213.

[28] S. Lee, I.N. Ivanov, J.K. Keum, H.N. Lee, Sci. Rep., 6 (2016) p 19621.

[29] G.I. Petrov, V. V. Yakovlev, J. Squier, Appl. Phys. Lett., 81 (2002) p 1023–1025.

[30] M. Pan, J. Liu, H. Zhong, S. Wang, Z.F. Li, X. Chen, W. Lu, J. Cryst. Growth., 268 (2004) p 178–183.

[31] L.S. Taylor, G. Zografi, Pharm. Res., 15 (1998) p 755–761.

[32] T. Ye, Z. Dong, Y. Zhao, J. Yu, F. Wang, S. Guo, Y. Zou, CrystEngComm., 13 (2011) p 3842.

[33] M.J. Miller, J. Wang, , J. Appl. Phys., 117 (2015).

[34] Y. Zhang, Y. Huang, Mater. Lett., 182 (2016) p 285–288.

[35] B. Akinwolemiwa, C. Peng, G.Z. Chen, , J. Electrochem. Soc., 162 (2015) p A5054–A5059.

[36] A. Laheäär, P. Przygocki, Q. Abbas, F. Béguin, Electrochem. Commun., 60 (2015) p 21–25.

[37] D. Jiang, Q. Xu, S. Meng, C. Xia, M. Chen, , J. Alloys Compd., 706 (2017) p 41–47.

[38] T.M. Masikhwa, M.J. Madito, A. Bello, J.K. Dangbegnon, N. Manyala, J. Colloid Interface Sci., 488 (2017) p 155–165.

[39] A.H. Shah, W. Zaid, A. Shah, U.A. Rana, H. Hussain, M.N. Ashiq, R. Qureshi, A. Badshah, M.A. Zia, H.-B. Kraatz, J. Electrochem. Soc., 162 (2014) p H115–H123.